photonics

MDPI

Article

Fast and Accurate Measurement of Hole Systems in Curved Surfaces

Ping Wang [1,2], Lingbao Kong [1,*], Huijun An [1], Minge Gao [1] and Hailong Cui [3]

[1] Shanghai Engineering Research Center of Ultra-Precision Optical Manufacturing, Fudan University, Shanghai 200438, China
[2] Institute of Machinery Manufacturing Technology, China Academy of Engineering Physics, Mianyang 621900, China
[3] Sichuan Precision and Ultra-Precision Machining Engineering Technology Center, Chengdu 610200, China
* Correspondence: lkong@fudan.edu.cn; Tel.: +86-21-31242565

Abstract: Curved surface structural parts with hole systems are widely used, and accurate measurement of the hole systems is crucial for assembly and functionality. This study presents a novel approach using machine vision and structural science principles to accurately measure spherical hole systems. We introduce key technologies, including measurement parameter definition, system design, and error modeling, in the paper. Our approach overcomes the limitations of existing methods, offering flexibility, precision, and automation measurement of the hole system. Experimental results demonstrate an accuracy of 0.348′ (arcminutes). This research contributes to the optical measurement of curved surface hole systems and improves their alignment and functionality.

Keywords: hole systems; curved surface; measurement parameters; optical measurement; error evaluation

check for updates

Citation: Wang, P.; Kong, L.; An, H.; Gao, M.; Cui, H. Fast and Accurate Measurement of Hole Systems in Curved Surfaces. *Photonics* **2023**, *10*, 1337. https://doi.org/10.3390/photonics10121337

Received: 9 October 2023
Revised: 21 November 2023
Accepted: 29 November 2023
Published: 2 December 2023

1. Introduction

Curved structural parts with hole systems are widely used in aerospace, automotive manufacturing, defense, and other fields [1]. These holes play a crucial role in aligning parts and enabling specific functions, leading to heightened research into the geometric characteristics of the hole system.

As industrial manufacturing technology advances, traditional contact measurement methods face limitations with complex surfaces and micro-hole positions. To meet the demands of precision manufacturing, researchers explore non-contact methods, employing machine vision and image processing to accurately measure hole system coordinates [1]. Through this method, the limitations of traditional measurement methods can be overcome. The application of these technologies has introduced more precise and reliable measurement methods to the engineering field, which provides better support for product design, processing, and assembly processes, ultimately elevating industrial manufacturing to a higher level of precision and quality.

In this field, researchers have developed various methods to measure the center coordinates of the holes in curved hole systems. For instance, Zhu et al. [2] utilized a linear array imaging system for high-precision measurements, accomplishing this by identifying hole centers and calculating diameters through image processing. Similarly, Huang et al. [3,4] accomplished sub-pixel center positioning through a non-contact linear array CCD system, achieving a center coordinate repetition accuracy of under 4μm by employing variable speed scanning and applying the least square method for circle fitting. Yu [5] integrated photoelectric technology and digital image processing to capture spherical circular hole images, introducing versatile acquisition methods for diverse measurement needs. Deng [6] realized high-precision two-dimensional image measurement through linear array mechanical scanning devices and grating positioning. Huang [7] optimized measurements by converting three-dimensional data into two-dimensional image identification. Moreover,

Zhang et al. [8] proposed a laser displacement-based solution for rapid spatial hole system measurement. Additionally, Xu [9] enhanced measurement accuracy by implementing a collimated laser beam-guided precise positioning method and self-focusing fiber collimation. Sun et al. [10] introduced a vision-based method for edge feature extraction and hole parameter calculation. Chen et al. [11] developed a dual sensor self-focusing method that combines optical vision sensors with tactile probes for automated measurement. In a software-driven approach, Xu et al. [12] managed measured part movement through C++ program, processed hole images in MATLAB, and achieved spatial position measurements using a mixed programming approach. Moreover, Long [13] proposed a projection-based hole system measurement method for rapid positioning and reduced inspection time. Chen et al. [14] presented an active dual sensor automatic focusing system tailored for aperture arrays on free-form surfaces.

After the measurement methods have been fully explored, many scholars have also analyzed the measurement errors. Li [15] optimized the reference coordinate system of a three-dimensional coordinate machine to reduce positional measurement errors. Huang et al. [16] proposed a method to measure the position error of the hole system with "hemispherical" auxiliary parts on the microscope. Huang et al. [17] developed a tool positioning and error verification system based on machine vision and used pixel calibration and image correlation to determine tool position error. Xie [18] employed an instrument combination method to measure angles between holes in large peripheral hole systems. Luo [19] studied the field measurement method error of different hole center spacing in the process of mold processing and manufacturing, and the results show that the error can be minimized by measuring the internal and external dimensions and calculating the average value. He et al. [20] assess composite position errors in spherical hole systems by calculating absolute position errors and employing optimization algorithms for relative position errors. Wang et al. [21] introduced a method for measuring concentricity errors in parts. They collected data using three-coordinate measurements, established a reference axis by fitting a section circle, and evaluated concentricity errors and uncertainties using a reference axis and measured hole data. Yu et al. [22] developed a system using a laser collimation beam and a biaxial dip sensor to evaluate coaxiality errors in non-reference hole systems. Addressing concentricity detection for diesel engine gear chamber cover holes, Wu [23] utilized pins and inspection tools for workplace positioning, using a clamping table mandrel to measure coordinate position errors and coaxiality errors relative to the pinholes. Xu [24] enhanced a large-distance distributed hole system, establishing a new coordinate system based on biaxial dip sensors, thus improving measurement speed, applicability, and accuracy. Furthermore, Xu [25] utilized the Newton interpolation method and a sub-pixel edge detection algorithm to measure position and coaxiality errors in small box hole systems.

In addition, 3D coordinate measurement of the hole system has been fully explored. Bieman et al. [26] achieved 3D hole location using backlight illumination, structural light technology, and structural light intersection. Gong et al. [27] employed machine vision and multi-view stereo vision for the 3D measurement of complex inner surfaces in online manufacturing. Liu [28] collected point cloud data using line structure light 3D measurement, enabling size and position measurement through point cloud boundary extraction and circular hole detection. Gorpas et al. [29] used binocular structured light to measure the volume of small pores and achieved accurate measurement through image enhancement, feature detection, and 3D reconstruction. Malasilicis et al. [30] proposed a machine vision system for 3D surface hole measurements in low-contrast industrial environments. Zeng et al. [31] used machine vision technology to realize automatic measurement of the effective firing area of a cartridge flash hole. Gou et al. [32] developed a machine vision detection system for five-axis numerical control machining, which can efficiently detect small holes on complex curved surfaces. Fang et al. [33] developed an optical non-contact measuring instrument to accurately measure hole diameter, ovality, and cylindricity from reflected images. Yang [34] addressed through hole measurement in shell parts using segmentation techniques and enhanced accuracy through manual ferrule and image splicing methods.

However, the optical non-contact high-precision measurement of curved surface hole systems is still in the early stage of research. Existing research on measuring hole systems consistently presents several limitations. In general, traditional coordinate measuring machine (CMM) methods use a contact-based approach, making them unable to measure blind holes, and the resolution is limited when dealing with smaller-sized apertures. Additionally, current machine vision-based methods face challenges due to a restricted field of view, limiting the effective measurement range for hole dimensions. Moreover, high-precision and real-time measurement is challenging, as data analysis and processing are often intricate and resource-intensive, especially when dealing with small apertures or high-precision hole systems. Finally, some methods rely on manual intervention, increasing uncertainty and reducing measurement efficiency.

For further advancement, this paper introduced a special composite measuring scheme that combines structural science and machine vision technology. In this approach, the proposed scheme employs machine vision technology, enabling rapid acquisition of measurement results through images and algorithms. The scheme is capable of measuring blind holes and through holes on workpieces, demonstrating a certain level of versatility. Additionally, the machine is entirely computer-controlled, reducing human intervention and achieving automated measurement. To validate the effectiveness of the proposed visual measurement system, a series of experiments on errors and uncertainties were conducted, and the measurement results were compared with those of a three-coordinate measurement device. The results indicate that the traditional three-coordinate measurement method takes over 30 min to complete one experiment, whereas the proposed measurement machine only requires 5 min, with a measurement difference of only 0.348 arcminutes compared to the three-coordinate machine. Our approach overcomes limitations in existing methods, offering high flexibility, high precision, and a high degree of automation. This research contributes to the optical measurement of curved surface hole systems, improving alignment and functionality.

2. Theoretical Fundamentals

The geometric model of spherical hole system coordinates shown in Figure 1 describes the conversion relationship between the imaging center point coordinates of the circular hole and the spatial included angle of its indexing, providing a theoretical basis for hole location coordinate measurement. Assuming hole A in Figure 1 is the reference hole for the location of the hole to be measured, a rectangular coordinate system, X, Y, and Z, is established through hole A and spherical orifice O. In accordance with Figure 1a, suppose a point C on the sphere has its projection point C_{XOY} on the XOY plane and C_{YOZ} on the YOZ plane. We define $\angle YOC_{XOY}$ as γ and $\angle AOC_{YOZ}$ as Ψ. Ideally, by rotating the sphere angles ψ and γ around the X and Z axes, we can precisely align hole C with hole A, so as to measure the accurate space angle. This rotating motion usually adopts closed-loop control. When the feedback element is accurate enough, it can ensure that the rotation error is far less than the manufacturing error. In other words, the rotational error can be accommodated within the range of equipment measurement errors.

However, due to the manufacturing error of the small hole in the manufacturing process, the center point of hole C usually will not completely coincide with the center point of hole A. When rotating the center point of hole C to point P by rotating the sphere ψ and γ angles around the X and Z axes, to establish the angular relationship between point P and the center point A of the reference hole, we need to introduce some auxiliary lines. On a sphere, arcs that do not pass through the center of the sphere but intersect its surface are defined as small arcs, while arcs that pass through the center of the sphere and intersect its surface are defined as large arcs. The following are the specific steps for introducing auxiliary lines:

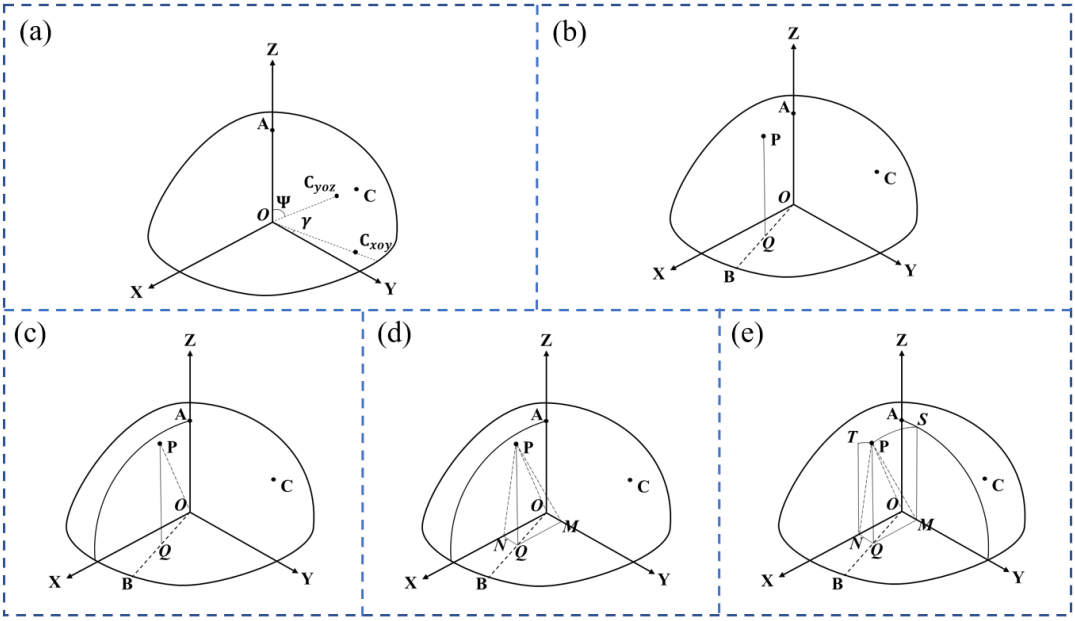

Figure 1. Geometrical model of the spherical hole system. (**a**) Positional relationship between point C and reference hole A. (**b**–**e**) Procedural steps for introducing auxiliary lines.

1. Draw a line PQ perpendicular to the coordinate plane XY at point Q. Additionally, draw a line OB through point Q intersecting a large arc on coordinate plane XY at point B, as shown in Figure 1b;
2. As shown in Figure 1c, draw a large arc AB passing through plane OAB, and point P must be on large arc AB and $OP = R$;
3. As shown in Figure 1d, draw a line QM perpendicular to the Y axis at point M and a straight line QN perpendicular to the X axis at point N;
4. Draw a line MS parallel to the Z axis, intersecting the large arc on the coordinate plane YZ at point S, and then the small arc of the plane $PQMS$ on the sphere is PS;
5. Draw a line NT parallel to the Z axis, intersecting the large arc on the coordinate plane XZ at point T, and the small of the plane $PQNT$ arc on the sphere is PT, as shown in Figure 1e.

Assuming $QM = a$ and $QN = b$:

$$OQ = \sqrt{QM^2 + QN^2} = \sqrt{a^2 + b^2} \tag{1}$$

$$PQ = \sqrt{OP^2 - OQ^2} = \sqrt{R^2 - (a^2 + b^2)} \tag{2}$$

$$PM = \sqrt{QM^2 + PQ^2} = \sqrt{a^2 + R^2 - (a^2 + b^2)} = \sqrt{R^2 - b^2} \tag{3}$$

$$PN = \sqrt{QN^2 + PQ^2} = \sqrt{b^2 + R^2 - (a^2 + b^2)} = \sqrt{R^2 - a^2} \tag{4}$$

$$\angle QON = arctan\frac{QN}{QM} = arctan\frac{b}{a} \tag{5}$$

$$\angle PNT = \angle QPN = arcsin\frac{QN}{PN} = arcsin\frac{b}{\sqrt{R^2 - a^2}} \tag{6}$$

$$\angle POA = \angle OPQ = arcsin\frac{OQ}{OP} = arcsin\frac{\sqrt{a^2 + b^2}}{R} \tag{7}$$

Obviously, point P is rotated around the X and Z axes to the reference point A position.

Specifically, the angle of rotation around the X axis $\theta = \angle PNT$, the angle of rotation around the Z axis $\lambda = \angle QON$, and the space angle between point P and datum point A is $\angle POA$.

To measure the coordinates of the whole spherical hole system, the center point coordinate value (X_0, Y_0) of the position of the reference hole A is firstly determined, and then the previously measured circular hole on the spherical surface is rotated (its center point is set as C). As point C cannot completely coincide with reference hole A, it is assumed that point C is rotated to point P, which is very close to reference point A. During this process, the angles of point C rotating to point P around the X and Z axes are ψ and γ (the angle is completed under the high-precision closed-loop control, with very small error, which can be regarded as a part of the measurement error). Finally, measure the circular hole and obtain the coordinate value of its center point P as (X, Y) and set the magnification of the optical imaging system as ρ; then:

$$a = (X - X_0)/\rho \tag{8}$$

$$b = (Y - Y_0)/\rho \tag{9}$$

$$\theta = \angle PNT = arcsin\frac{b}{\sqrt{R^2 - a^2}} = arcsin\frac{Y - Y_0}{\sqrt{\rho^2 R^2 - (X - X_0)^2}} \tag{10}$$

$$\lambda = \angle QON = arctan\frac{b}{a} = arctan\frac{Y - Y_0}{X - X_0} \tag{11}$$

Let α and β represent the angles of rotation around the X and Z axes from the center of measured circular hole C to the center of reference hole A. Then, α and β can be determined from θ, ψ, and λ, γ as follows:

$$\begin{cases} \alpha = \psi + \theta \\ \beta = \gamma + \lambda \end{cases} \tag{12}$$

That is:

$$\begin{cases} \alpha = \psi + arcsin\frac{Y - Y_0}{\sqrt{\rho^2 R^2 - (X - X_0)^2}} \\ \beta = \gamma + arctan\frac{Y - Y_0}{X - X_0} \end{cases} \tag{13}$$

In the actual measurement, the values of $X - X_0$ and $Y - Y_0$ (normally below 300 μm) are far less than ρR, which can be ignored in the denominator in Equation (13), so the above formula can be simplified as:

$$\begin{cases} \alpha = \psi + arcsin\frac{Y - Y_0}{\rho R} \\ \beta = \gamma + arctan\frac{Y - Y_0}{X - X_0} \end{cases} \tag{14}$$

where α, β, ψ, and γ are measured in radian, ρ is the magnification of the optical path system, R is the radius of the sphere, and (X_0,Y_0) and (X,Y) are the coordinate values of the reference hole and the measured hole center obtained by the image recognition, and the unit is a micrometer. In Equation (14), it can be seen that when the sphere rotates in place (i.e., the angles of the sphere rotating around the X and Z axes and ψ and γ are known), measure the coordinate difference $(X - X_0)$ and $(Y - Y_0)$ between the spherical circular hole and the reference hole in the X and Y directions, and then any angles α, β that are needed can rotate from the circular hole on the spherical surface to the reference hole around the X axis and Z axis.

From the above analysis, the measurement of the spatial angle deviation of the hole can be converted into the measurement of the hole system center. In order to measure the center of the hole, it is only necessary to collect images of the circular hole after the rotation is completed, and then a machine vision algorithm can be used to identify the center of the circle and calculate the coordinates of the hole. Then, the hole coordinate deviation between the hole to be measured and the reference hole can be converted into angle deviation to complete the precision and manufacturing error analysis.

3. Measurement Scheme and Error Analysis of the Holes in a Spherical Surface

3.1. Overall Measurement Scheme

In order to perform the measurement of the curved surface holes, it is necessary to select an appropriate basic configuration. Typical configurations include a cradle turntable forming a five-axis measuring machine [35], a cradle turret optical measurement machine [36], and a composite special measuring unit [37]. The five-axis measuring unit containing a cradle turntable has the flexibility of multi-axis movement and can rotate in multiple directions. However, this supplementary mechanical movement introduces a significant amount of error, which ultimately impacts the accuracy of the measurements. The optical measuring machine of the cradle turntable utilizes the high-precision features of optical measurement. However, its ability to rotate in multiple degrees of freedom is limited, preventing it from conducting measurements in multiple directions. In comparison, the composite measurement machine combines the advantages of mechanical motion and optical measurement and has multi-degree freedom, automated measurement capability, high accuracy, stability, and reliability, and is more suitable for the measurement of curved surface holes. Therefore, we used the composite measuring machine as the basic configuration. The overall principle framework is shown in Figure 2.

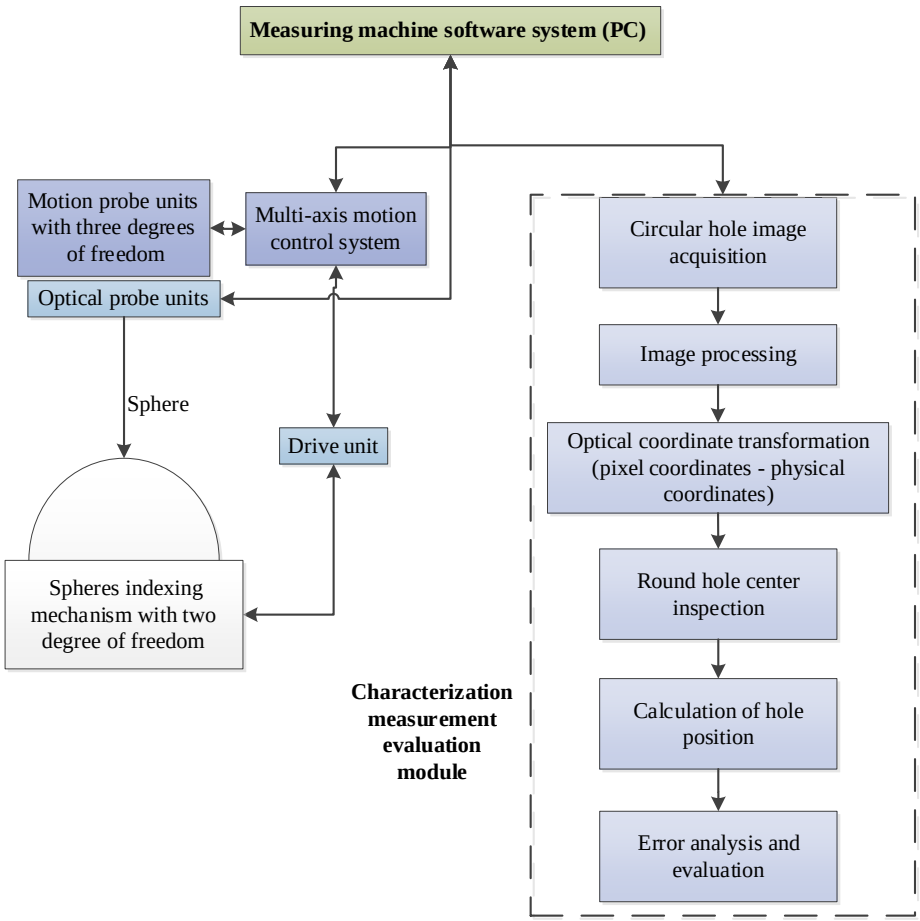

Figure 2. Overall principle frame diagram of the measuring machine.

From the derivation of the spherical coordinate system in Section 2, we know that the core element of measuring a spherical coordinate system is measuring the radius and two rotation angles. To meet the measurement requirements of the spherical aperture system, it is necessary to establish two rotational degrees of freedom: longitude and latitude. At the same time, the measuring radius is determined by the contour radius of the part to be measured. To ensure that the measuring machine can adapt to the spherical hole system with different radii, we introduce the multi-axis motion control system. In this measuring

system, the optical probe can realize the motion and detection of two degrees for freedom, and the sphere to be measured is fixed on a rotating table.

In order to realize automatic measurement and reduce manual intervention, the whole measurement process is completed under the control of the upper computer. The measurement process is as follows. The upper computer sends measurement commands to guide the multi-axis motion control system to work cooperatively. It first drives the turntable to rotate, and at the same time controls the motion unit of the measuring head to move the optical measuring head to a proper angle and position, so that the optical measuring head captures the spherical surface image and transmits it to the upper computer. The measurement machine based on optical probe technology essentially converts the 3D measurement task into 2D image processing and then uses the 2D image processing results to calculate the 3D angle in space. First, the upper computer processes the received image data captured by the optical probe, including image denoising, enhancement, distortion removal, etc. Then, the measurement software converts the pixel coordinates of the hole system image taken in the image into physical coordinates and maps the points in the image to the actual measurement space. Next, the system detects the center of the circular hole and calculates the angle deviation between the hole being measured and the reference hole according to the center coordinates of the circular hole. Finally, the system performs an error analysis and evaluation to evaluate the accuracy of the measurement results.

The general layout of the special measuring setup is shown in Figure 3. The special measuring unit is mainly composed of a mechanical system, a control system, and a measuring system. The mechanical system includes a high-stability lathe body, a measuring head support (rocker arm) and a location adjustment unit, a mechanical A-axis turntable unit, a part clamping and adjustment unit, a C-axis air-floating turntable, an air circuit processing unit, a vibration isolation unit. The control system includes a two-axis motion master control unit and a drive unit, an equipment status monitoring and its auxiliary control unit, a human interaction module, an equipment error compensation unit, and a head integrated management unit. The measurement system mainly includes a precision measuring head and a calibration unit, a feature measurement and an evaluation unit, and multi-function measurement software developed based on the PC+UMAC control system.

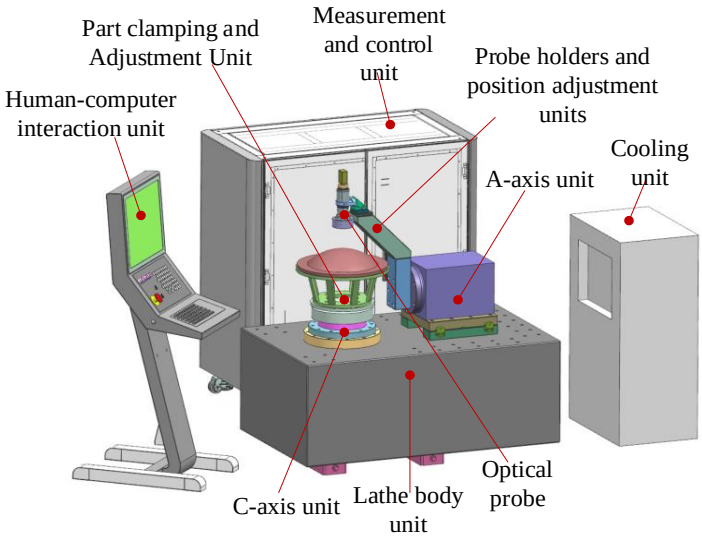

Figure 3. The general layout of a special measuring machine.

The sphere indexing mechanism is mainly composed of an A/C dual turntable. The A-axis and C-axis turntables are installed on the bed unit as two independent motion mechanisms. Parts can be rotated with one degree of freedom driven by the C-axis, and the optical measuring head can be rotated with another degree of freedom driven by the A-axis. The two rotation axes A and C vertically intersect with each other. The intersection of the two axes serves as the sphere center of the part to be measured. The axis of the optical

measuring head points to the center of the sphere, and the design basis of the measurement platform is thus established.

During measurement, it is necessary to adjust the altitude of the parts and establish them in conjunction with the machining datum of the parts to be measured. Additionally, auxiliary detection means should be constructed to detect the motion deviation of the surface contour of the parts along axes A and C separately. To ensure accuracy, the leveling and centering mechanism, as well as the height adjustment mechanism, should be utilized to ensure that the intersection point of the two axes aligns (or nearly aligns) with the sphere center of the parts being measured, and the reference hole of the parts being machined should be located at the rotation center of the C-axis. In addition, it is also necessary to establish a measurement programming reference for the part based on its machining reference to ensure the accuracy and consistency of the measurement results.

3.2. Measurement Error Analysis and Shafting Optimization

With this measuring machine, the holes in a spherical surface part are taken as the measuring objective. We need to evaluate the impact of various errors as cumulative errors of the entire machine, clarify the key error items that affect the measurement most critically, and then evaluate the balance of the measurement error in order to provide a reasonable allocation of various accuracies for the entire machine.

The errors in the measuring machine can be classified into two types: geometrical errors and positional errors. Each axis exhibits six geometric errors, comprising three translational and three angular errors. Positional errors depict the deviation between the actual and ideal positions of the axis, while angular errors represent the disparity between the actual and ideal orientations of the axis. The error components within the measuring machine are presented in Table 1.

Table 1. Measuring machine error components.

Number	Component	Meaning of Component
1	EXA	A-Axis X-Direction Position Error
2	EYA	A-Axis Y-Direction Position Error
3	EZA	A-Axis Z-Direction Position Error
4	EAA	A-Axis Angular Positioning Error
5	EBA	A-Axis Angular Error around the Y Direction
6	ECA	A-Axis Angular Error around the Z Direction
7	EXC	C-Axis X-Direction Position Error
8	EYC	C-Axis Y-Direction Position Error
9	EZC	C-Axis Z-Direction Position Error
10	EAC	C-Axis Angular Error around the X Direction
11	EBC	C-Axis Angular Error around the Y Direction
12	ECC	C Axis Angular Positioning Error
13	BOA	Parallelism of the A-Axis with the XZ Plane
14	COA	Parallelism of the A-Axis with the XY Plane
15	YOA	Eccentricity of the A-Axis in the Y Direction
16	ZOA	Eccentricity of the A-Axis in the Z Direction
17	AOC	Parallelism of the C-Axis with the YZ Plane
18	BOC	Parallelism of the C-Axis with the XZ Plane
19	XOC	Eccentricity of the C-Axis in the X Direction
20	YOC	Eccentricity of the C-Axis in the Y Direction
21	EXW	Workpiece Clamping X-Direction Position Error
22	EYW	Workpiece Clamping Y-Direction Position Error
23	EZW	Workpiece Clamping Z-Direction Position Error
24	EAW	Workpiece Clamping Angular Deviation around the X Direction
25	EBW	Workpiece Clamping Angular Deviation around the Y Direction
26	ECW	Workpiece Clamping Angular Deviation around the Z Direction

Using axis A as an illustration, Figure 4 illustrates the six geometrical errors for axis A.

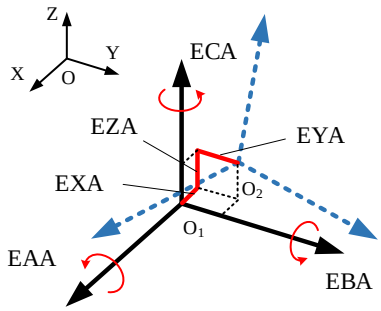

Figure 4. Position-related errors of Axis A.

The positional errors primarily involve the parallelism error and positional error of the rotational axis relative to the ideal axis. Figure 5 depicts the positional errors for rotational axes A and C.

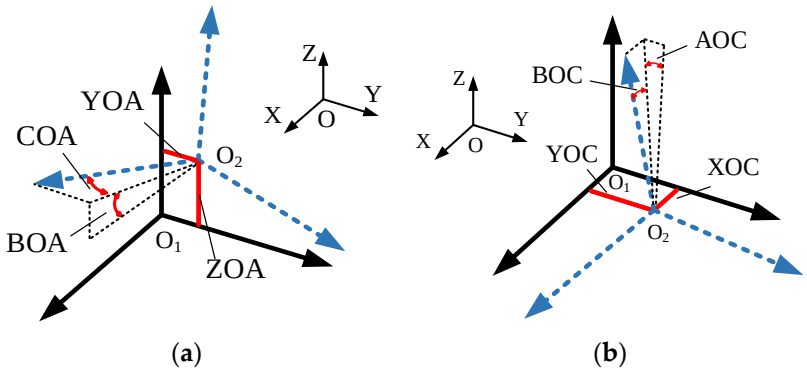

Figure 5. Positional errors. (**a**) Positional errors for axis A. (**b**) Positional errors for axis C.

The geometrical and positional errors of the measurement machine can be determined through an analysis of its topological structure and the principles governing error propagation, as illustrated in Equation (15) to Equation (19).

$$G_C = \begin{bmatrix} 1 & 0 & \mathrm{BOC} & \mathrm{XOC} \\ 0 & 1 & -\mathrm{AOC} & \mathrm{YOC} \\ -\mathrm{BOC} & \mathrm{AOC} & 1 & 0 \\ 0 & 0 & 0 & 1 \end{bmatrix} \begin{bmatrix} cos(C) & -sin(C) & 0 & 0 \\ sin(C) & cos(C) & 0 & 0 \\ 0 & 0 & 1 & 0 \\ 0 & 0 & 0 & 1 \end{bmatrix} \begin{bmatrix} 1 & -\mathrm{ECC} & \mathrm{EBC} & \mathrm{EXC} \\ \mathrm{ECC} & 1 & -\mathrm{EAC} & \mathrm{EYC} \\ -\mathrm{EBC} & \mathrm{EAC} & 1 & \mathrm{EZC} \\ 0 & 0 & 0 & 1 \end{bmatrix} \tag{15}$$

$$T_C = \begin{bmatrix} 1 & 0 & 0 & d_{ca}^{p} \\ 0 & 1 & 0 & 0 \\ 0 & 0 & 1 & 0 \\ 0 & 0 & 0 & 1 \end{bmatrix} \tag{16}$$

$$G_A = \begin{bmatrix} 1 & -\mathrm{COA} & \mathrm{BOA} & 0 \\ \mathrm{COA} & 1 & 0 & \mathrm{YOA} \\ -\mathrm{BOA} & 0 & 1 & \mathrm{ZOA} \\ 0 & 0 & 0 & 1 \end{bmatrix} \begin{bmatrix} 1 & 0 & 0 & 0 \\ 0 & cos(A) & -sin(A) & 0 \\ 0 & sin(A) & cos(A) & 0 \\ 0 & 0 & 0 & 1 \end{bmatrix} \begin{bmatrix} 1 & -\mathrm{ECA} & \mathrm{EBA} & \mathrm{EXA} \\ \mathrm{ECA} & 1 & -\mathrm{EAA} & \mathrm{EYA} \\ -\mathrm{EBA} & \mathrm{EAA} & 1 & \mathrm{EZA} \\ 0 & 0 & 0 & 1 \end{bmatrix} \tag{17}$$

$$T_A = \begin{bmatrix} 1 & 0 & 0 & d_{ao}^{p} \\ 0 & 1 & 0 & 0 \\ 0 & 0 & 1 & d_{ao}^{v} \\ 0 & 0 & 0 & 1 \end{bmatrix} \tag{18}$$

$$T_W = \begin{bmatrix} 1 & -ECW & EBW & EXW \\ ECW & 1 & -EAW & EYW \\ -EBW & EAW & 1 & EZW \\ 0 & 0 & 0 & 1 \end{bmatrix} \tag{19}$$

The overall measurement error of the entire machine can be expressed as:

$$P_{err}^{W} = P_{actual}^{W} - P_{ideal}^{W} \tag{20}$$

where:

$$\begin{cases} P_{actual}^{W} = (G_c T_W)^{-1} T_c G_A T_A P \\ P_{ideal}^{W} = (G_c)^{-1} T_c G_A T_A P \end{cases} \tag{21}$$

where G_C represents the geometric error caused by the C-axis, G_A represents the geometric error caused by the A-axis, T_C represents the displacement error caused by the C-axis, T_A represents the displacement error caused by the A-axis, d_{ao}^{p} represents the horizontal span between the A-axis coordinate system and the probe coordinate system, d_{ao}^{v} represents the vertical span between the A-axis coordinate system and the probe coordinate system, d_{ca}^{p} represents the horizontal span between the A-axis and C-axis coordinate systems, T_W represents the error introduced during the workpiece clamping process, and P represents the actual measured coordinates of the hole in the world coordinate system.

The error measurement process is shown in Figure 6. Firstly, it is necessary to establish a part model, determine the theoretical position distribution of the measured part features, and obtain the theoretical target position of the optical measuring head. Upon obtaining the theoretical position distribution of each axis in the machine coordinate system using the kinematic model, we input the initial error parameters specified in the design requirements of the measuring machine. By combining this input with the geometric error model of the entire machine, we can determine the actual position of the measuring head, accounting for error accumulation. Since the final assessment of the angle error is contingent upon the center point of the spherical circular hole in the 2D vertical projection plane, we project the actual position of the probe onto the sphere to ascertain the projection point. Subsequently, we calculate the measurement deviation of the spherical center angle caused by geometric error transmission. This calculation is based on the projection point of the probe and the theoretical target position point. Finally, we evaluate the measurement error according to relevant criteria.

(1) The position distribution model for detecting features

Due to the varying degrees of cumulative detection errors of measuring machines at different detection positions, it is necessary to clarify the theoretical position distribution of each axis in the machine coordinate system for specific detection feature position distribution in order to obtain the individual error corresponding to each detection feature position. Subsequently, we analyze the impact of individual errors on the measurement accuracy of the entire machine (error sensitivity). To achieve this objective, we focus on a specific spherical analog component and select positions distributed uniformly on the hemispherical surface, as illustrated in Figure 7, as representative measurement features. We use these features to analyze the error impact of the measuring machine.

Based on the kinematic model of the measuring machine established in Section 2 of this article and the definition method of spherical longitude and latitude, the position distribution of each axis of the measuring machine in machine coordinates corresponding to the spherical feature position in each component coordinate system can be solved.

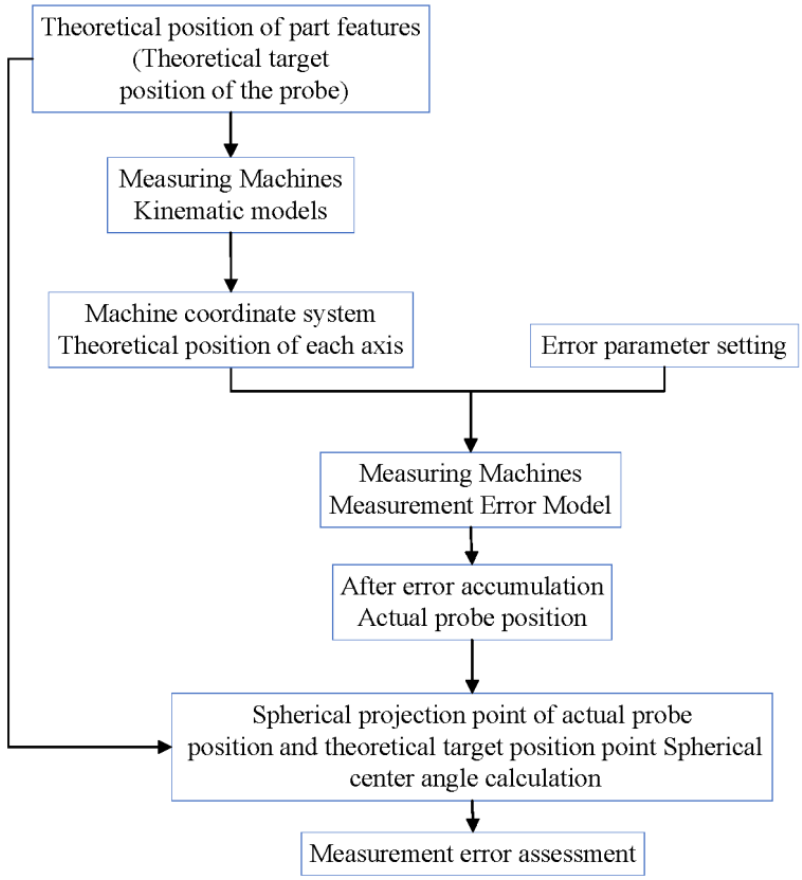

Figure 6. Flowchart of measurement error impact analysis.

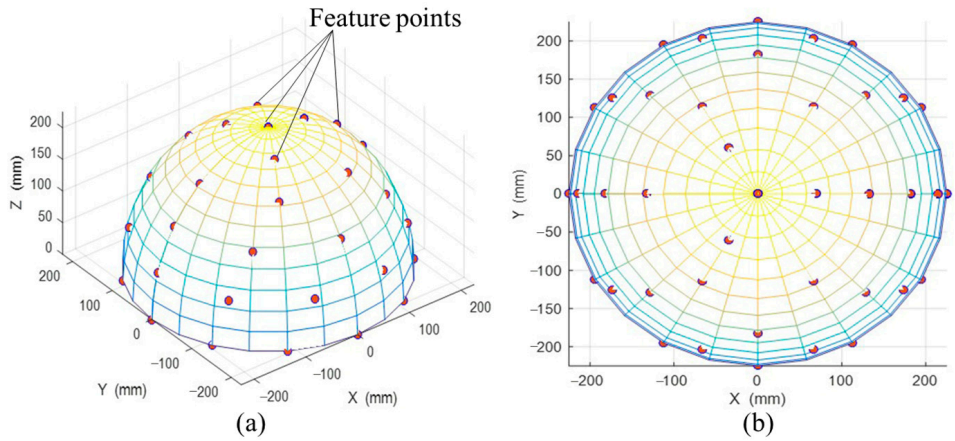

Figure 7. Typical feature selection of spherical components. (**a**) Stereoscopic view (**b**) Top view.

(2) Evaluation method of measurement error

Assuming that the ideal detection point position of the part to be tested is located directly above the part, the probe should be located directly above the part and completely perpendicular to the part. However, according to the geometric error model of the measuring machine, during the transformation process of the part coordinate system, the position coordinates of the probe will be added to transmission errors, resulting in the probe being unable to accurately locate the theoretical position of the feature to be tested based on the attitude adjustment of the rotation axis; that is to say, the ideal position and the actual position of the probe will not completely coincide, as shown in Figure 8.

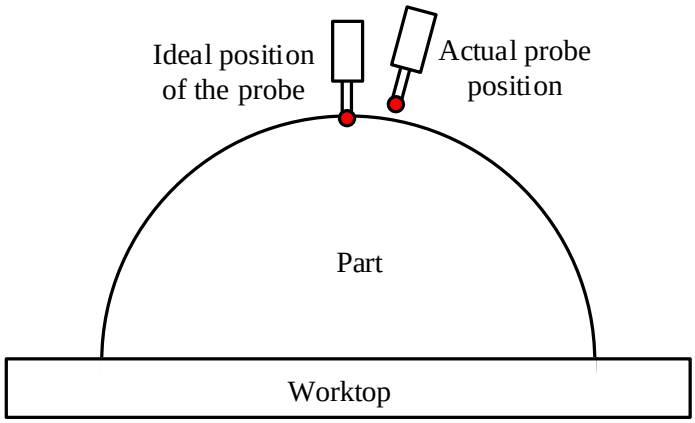

Figure 8. Schematic diagram of measurement error in the coordinate system of the part.

In our measurement experiment, a non-contact probe with a working distance of D is employed. To enhance the accuracy of feature point projection and reduce uncertainty in error evaluation, we treat the working distance of non-contact probes as part of the length of contact probes. Thus, when determining the actual detection position, the actual probe position was simply projected onto the ideal sphere in the normal direction to obtain the actual detection position point.

For evaluating part characterization errors, the ultimate measurement objective is to determine the angular deviation between the ideal detection point and the actual detection point. To achieve this goal, it is necessary to convert the positional coordinate deviation of the measuring point within the spherical coordinate system of the part into the angular deviation relative to the spherical center shown in Figure 9 according to Equation (14).

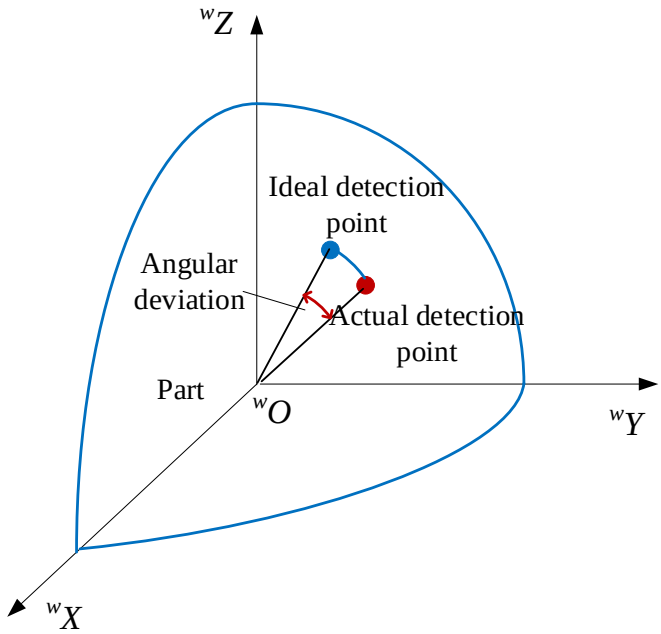

Figure 9. Schematic diagram of the deviation angle of hole position detection.

3.3. Accuracy Allocation of the Measurement Machine

(1) Geometric error allocation of measuring machines

Based on the existing technical level and engineering practice experience, the initial values of various geometric errors were selected as inputs for the overall measurement geometric error model, and the degree of error impact of the measuring machine was

analyzed. Finally, the overall geometric error allocation of the measuring machine was determined, as shown in Table 2.

Table 2. Geometric accuracy allocation requirements for measuring machines.

Index	Precision Distribution
Stroke of axis A	$\pm 90°$
Rotation error of axis A	1 μm
End tripping of axis A	1 μm
Angular runout of axis A	1.5 μm/300 mm(5×10^{-6} rad)
Rotation error of axis C	30 nm
End tripping of axis A	30 nm
Angular runout of axis C	1.5 μm/300 mm(5×10^{-6} rad)
Installation parallelism of axis A	3 μm/300 mm(1×10^{-5} rad)
Installation translation deviation of axis A	3 μm
Installation parallelism of axis C	3 μm/300 mm(1×10^{-5} rad)
Part clamping angle deviation	3.5×10^{-5} rad
Part clamping position translational deviation	10 μm

(2) Allocation of measurement accuracy for optical probes

This system uses an optical probe as a hole system feature recognition device, which will introduce measurement errors in the optical system, including camera resolution errors, optical lens distortion errors, image processing algorithm errors, etc.

The resolution error of the camera is limited by the hardware performance indicators of the camera. At present, the measuring head of a commercial industrial camera can realize 2 μm to 3 μm optical resolution under a 6 mm × 6 mm field of view and can calculate with a measurement resolution accuracy of 5 μm, which may result in a measurement angle deviation of approximately 4″ (0.07′) for specific parts.

The optical lens distortion error can be reduced by selecting a large-aperture optical lens to reduce the imaging error at the lens edge while using optical image correction to further weaken this error. Therefore, the impact of this error can be ignored.

The error associated with image processing algorithms refers to inaccuracies introduced during various image processing stages, including data processing, edge extraction, feature recognition, and hole center searching from captured camera images. According to reference [38], the magnitude of this angle error is on the order of several milliseconds and can be disregarded. Consequently, the primary source of measurement error in the probe stems from the camera's resolution error. To assess the system's measurement error, the initial value of the probe angle measurement error is set to 5″ (0.083′).

(3) Comprehensive measurement accuracy analysis

Comprehensive measurement error enables us to quantify the overall accuracy of the measurement equipment under specific initial conditions. To calculate this error in this study, we employed the error synthesis rule, which involves the consideration of individual error sources. These individual error sources were collectively assessed by summing the squares of their values and subsequently taking the square root to derive the comprehensive error.

According to the measurement error analysis flow shown in Figure 6, we made multiple measurements of the individual errors listed in Table 1 for all the component detection features shown in Figure 7; the specific analysis results are shown in Table 3.

By incorporating the error terms from Table 3 into Equation (20), the maximum overall measurement error of the measuring machine is 0.73′, and the measurement error of the probe is around 0.083′. According to the error synthesis rule, the comprehensive measurement error of the entire equipment under the current initial value conditions is about 0.735′ ($\sqrt{0.73^2 + 0.083^2}$).

Table 3. Effect of error components for the entire machine.

Number	Component	Average Measurement Error	Maximum Measurement Error
1	EXA	0.0305	0.0317
2	EYA	0.0211	0.0332
3	EZA	0.0162	0.0291
4	EAA	0.0515	0.0757
5	EBA	0.1812	0.2117
6	ECA	0.1064	0.1553
7	EXC	7.66×10^{-4}	0.0036
8	EYC	8.92×10^{-4}	0.0029
9	EZC	7.89×10^{-4}	0.0026
10	EAC	0.0231	0.0397
11	EBC	0.0236	0.0397
12	ECC	0.0582	0.0743
13	BOA	0.0338	0.0776
14	COA	0.0602	0.0787
15	YOA	0.1269	0.1283
16	ZOA	0.1273	0.1293
17	AOC	0	0
18	BOC	0	0
19	XOC	0	0
20	YOC	0	0
21	EXW	0.162	0.269
22	EYW	0.165	0.269
23	EZW	0.210	0.267
24	EAW	0.113	0.155
25	EBW	0.121	0.155
26	ECW	0.120	0.153

4. Measurement System and Testing

The optical probe utilizes a non-coaxial illumination configuration with a MORITEX lens (model MML1.5-HR110VI-35F). The lens has a field of view size of 8.5 mm × 6.4 mm, a resolution of 2.9 microns, and a depth of field of 0.23 mm. In practical measurements, the object distance is 340.1 mm and the working distance is 109 mm.

4.1. Establishing an Optical Measurement Coordinate System

Place the calibrated workpiece on the C-axis and use clamping and adjustment units and high-precision displacement sensors to assist in aligning and leveling the parts so that the intersection point of the sphere center of the part and the 2D rotation axis coincide. Adjust the working distance between the optical lens and the parts to achieve optical focusing and adjust the camera posture to make the center of the calibrated workpiece reference hole position coincide with the center of the camera's field of view as much as possible. Start the optical system to measure the center coordinates of the standard hole position and move the current optical coordinate system to make the measurement result show (0,0) for the center coordinates of the standard hole position. The flowchart of the calibration of the workpiece reference hole position is shown in Figure 10.

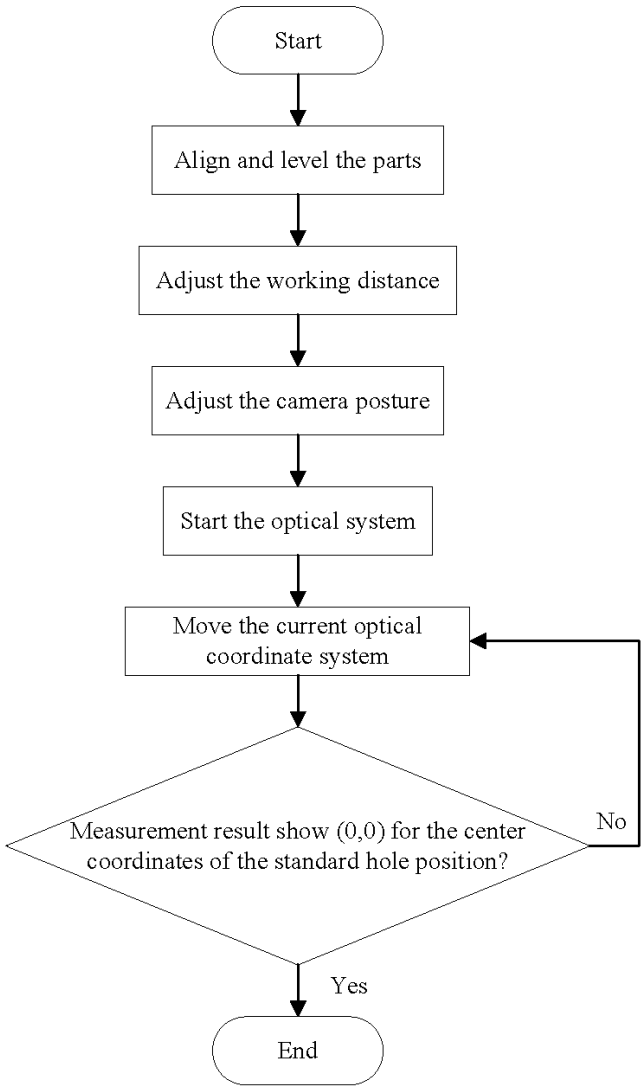

Figure 10. Flowchart of the calibration of the workpiece reference hole position.

4.2. Spherical Hole Positioning Based on the Machine Vision Algorithm

The tested component contains two types of holes: through holes and blind holes. Figure 11a presents the through hole on the tested component, and Figure 11d shows the blind hole. It can be visually observed that the interior part of the through hole spherical cavity (image foreground) appears dark in the image due to non-reflectivity, while the outer spherical region of the circular hole appears light (image background), making the circular hole features distinct. In the blind hole image, it can be seen that the reflection at the bottom of the blind hole causes the features inside the hole to resemble those of the outer spherical region, resulting in less distinct internal features. Figure 11b,e depict the grayscale histograms of the through hole and blind hole images, respectively. It can be noted that the histogram of the through hole image has two very distinct peaks, allowing for straightforward threshold segmentation to obtain the through hole region, as shown in Figure 11c. However, in the case of the blind hole, its histogram indicates a lack of a clear demarcation line between the image's foreground and background. The threshold segmentation results in Figure 11d are shown in Figure 11f.

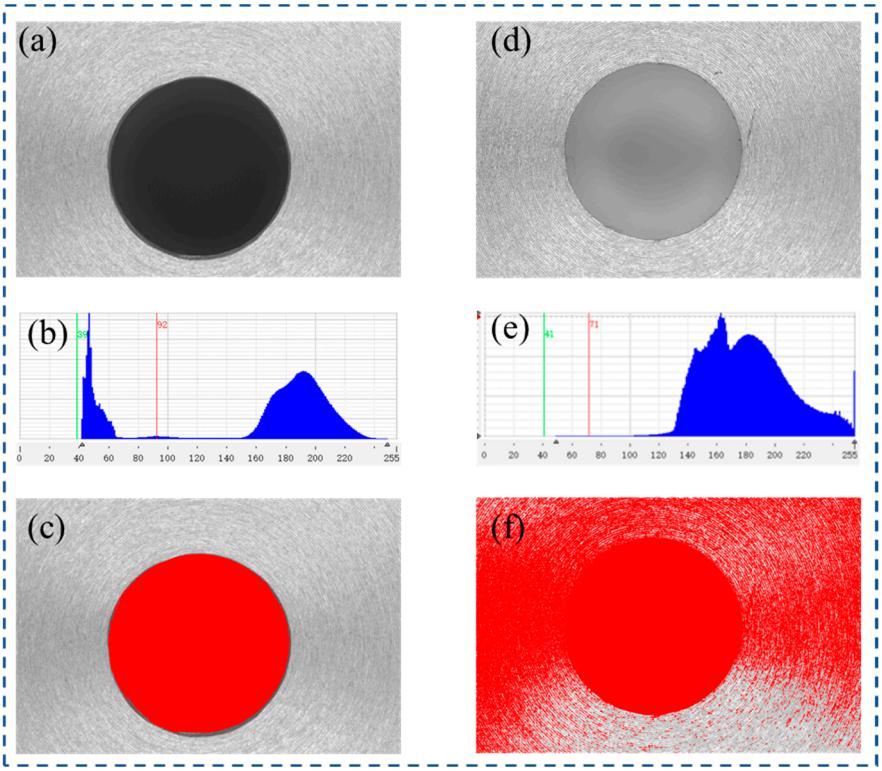

Figure 11. Images of through holes and blind holes on the test component. (**a**) Image of a through hole. (**b**) Grayscale histogram of a through hole image. (**c**) The through hole region after threshold segmentation. (**d**) Image of a blind hole. (**e**) Grayscale histogram of a blind hole image. (**f**) The blind hole region after threshold segmentation.

To achieve blind hole recognition, we employed a local thresholding method for image segmentation. The fundamental steps of the algorithm are as follows:

(1) Firstly, we performed mean filtering on the original image to obtain a smoothed reference image I_0, as shown in Figure 12a.

(2) Subsequently, we extracted the darker portions of the original image concerning the reference image using Equation (22), denoting the foreground (region of the blind hole) and the background (area outside the hole). The results of the local threshold segmentation are illustrated in Figure 12b.

$$I(x,y) = \begin{cases} foreground & I(x,y) \leq I_0(x,y) - T \\ background & I(x,y) \geq I_0(x,y) - T \end{cases} \tag{22}$$

where "foreground" represents the region of the blind hole, "background" represents the background area outside the hole, $I(x,y)$ denotes the pixel value at coordinates (x,y) in the original image, $I_0(x,y)$ represents the pixel value at coordinates (x,y) in the reference image, and the parameter T is chosen based on engineering experience. A larger T value results in a smaller extracted region.

(3) Finally, we performed region filling on the image obtained after local threshold segmentation, as shown in Figure 12c. Subsequently, we extracted the largest connected component, which represents the region of the blind hole, as illustrated in Figure 12d.

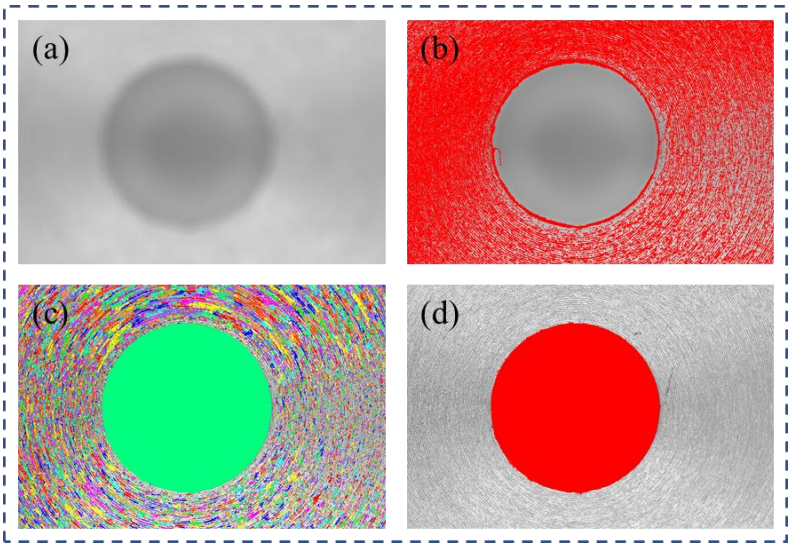

Figure 12. Blind hole region extraction. (**a**) Reference image I_0. (**b**) Local threshold segmentation. (**c**) Region filling and connected component segmentation. (**d**) Extracted blind hole region.

After identifying through holes and blind holes, it is necessary to precisely determine the center coordinates and radius of the test hole. Firstly, the Hough Circle Transform method is employed to locate the maximum inscribed circle in the foreground of the image. Assuming the center coordinates of the inscribed circle are (a, b) and the radius is R, the equation of the circle can be expressed as Equation (23).

$$(x-a)^2 + (y-b)^2 = R^2 \tag{23}$$

Expanding Equation (24) into a general form, it can be expressed as Equation (23):

$$x^2 + y^2 + Ax + By + C = 0 \tag{24}$$

where $A = -2a$, $B = -2b$, and $C = a^2 + b^2 - R^2$. When the number of points (x_i, y_i) on the edge of the through hole or blind hole region exceeds three, the coordinates of the measurement points cannot all satisfy Equation (24), indicating the existence of a residual error e_i between (x_i, y_i) and Equation (24), and e_i can be expressed as:

$$e_i = x_i^2 + y_i^2 + Ax_i + By_i + C \tag{25}$$

According to the characteristics of random errors, residuals tend to cancel each other out in positive and negative directions. To minimize residuals, it is necessary to square the errors, sum their squares, and minimize this sum. Following this principle, Equation (25) is transformed into a multivariate function with A, B, and C as unknowns, as shown in Equation (26).

$$f(A, B, C) = \sum_{i=1}^{n} {e_i}^2 = \sum_{i=1}^{n} \left(x_i^2 + y_i^2 + Ax_i + By_i + C\right)^2 \tag{26}$$

The extremum conditions for Equation (26) are:

$$\begin{cases} \frac{\partial f(A,B,C)}{\partial A} = 0 \\ \frac{\partial f(A,B,C)}{\partial B} = 0 \\ \frac{\partial f(A,B,C)}{\partial C} = 0 \end{cases} \tag{27}$$

Combining Equations (26) and (27), we obtain:

$$\begin{cases} 2\sum_{i=1}^{n}\left(x_i^2+y_i^2+Ax_i+By_i+C\right)\cdot x_i=0 \\ 2\sum_{i=1}^{n}\left(x_i^2+y_i^2+Ax_i+By_i+C\right)\cdot y_i=0 \\ 2\sum_{i=1}^{n}\left(x_i^2+y_i^2+Ax_i+By_i+C\right)\cdot 1=0 \end{cases} \tag{28}$$

Expanding and rearranging Equation (28), we obtain:

$$\begin{cases} A\cdot\sum_{i=1}^{n}x_i^2+B\cdot\sum_{i=1}^{n}x_iy_i+C\cdot\sum_{i=1}^{n}x_i=-\sum_{i=1}^{n}\left({x_i}^3+x_i{y_i}^2\right) \\ A\cdot\sum_{i=1}^{n}x_iy_i+B\cdot\sum_{i=1}^{n}{y_i}^2+C\cdot\sum_{i=1}^{n}y_i=-\sum_{i=1}^{n}\left({x_i}^2y_i+{y_i}^3\right) \\ A\cdot\sum_{i=1}^{n}x_i+B\cdot\sum_{i=1}^{n}y_i+C\cdot n=-\sum_{i=1}^{n}\left({x_i}^2+{y_i}^2\right) \end{cases} \tag{29}$$

The least squares solution for A, B, and C is:

$$\begin{bmatrix} A \\ B \\ C \end{bmatrix}=\begin{bmatrix} \sum_{i=1}^{n}x_i^2 & \sum_{i=1}^{n}x_iy_i & \sum_{i=1}^{n}x_i \\ \sum_{i=1}^{n}x_iy_i & \sum_{i=1}^{n}y_i^2 & \sum_{i=1}^{n}y_i \\ \sum_{i=1}^{n}x_i & \sum_{i=1}^{n}y_i & n \end{bmatrix}^{-1}\cdot\begin{bmatrix} -\sum_{i=1}^{n}\left({x_i}^3+x_i{y_i}^2\right) \\ -\sum_{i=1}^{n}\left({x_i}^2y_i+{y_i}^3\right) \\ -\sum_{i=1}^{n}\left({x_i}^2+{y_i}^2\right) \end{bmatrix} \tag{30}$$

The values obtained for A, B, and C from the above equation can be used to calculate the coordinates of the center (a, b) and the radius R of the circle:

$$a=-A/2,\ b=-B/2,\ R=\sqrt{a^2+b^2-C} \tag{31}$$

The coordinates of the center and radius of the through hole shown in Figure 11 are illustrated in Figure 13.

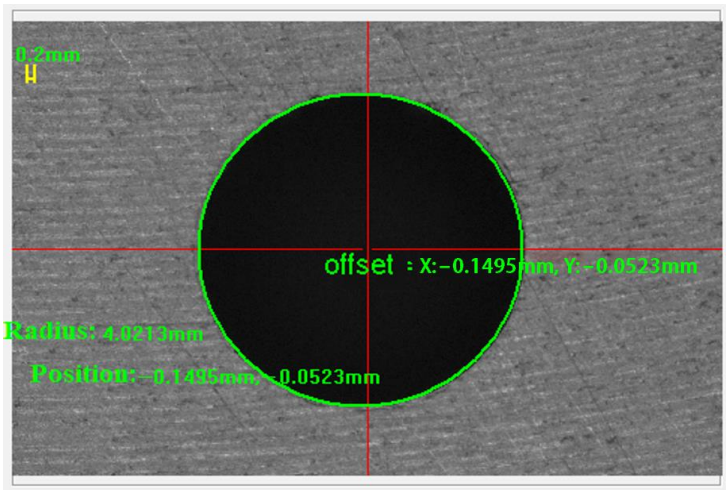

Figure 13. Measurement results of the through hole center coordinates and radius.

4.3. Measurement Process

Firstly, the orientation of the test workpiece is adjusted, and its sphere center is aligned with the intersection point of the C-axis and A-axis rotation axes. This step necessitates iterative adjustments to the workpiece orientation based on measurement outcomes. Ideally,

the longitude and latitude curves should converge toward an infinite straight line. Adjust the camera posture so that the center coordinate of the standard hole position of the workpiece is infinitely close to the intersection point of the coordinate system "cross line" and measure the deviation (X_0, Y_0) of the reference hole position at this time. The longitude starting point for measurement programming is constructed by combining the reference coordinates (X_0, Y_0) and the corresponding C-axis feedback angle constructed by combining other hole positions on the same longitude. The A-axis feedback angle corresponding to the construction of the reference coordinates (X_0, Y_0) is used as the latitude starting point for measurement programming, so the measurement programming datum is, therefore, constructed. The software interface for measuring the deviation of the camera reference hole position is shown in Figure 13. A high-precision displacement sensor assists in workpiece leveling and centering, as shown in Figure 14.

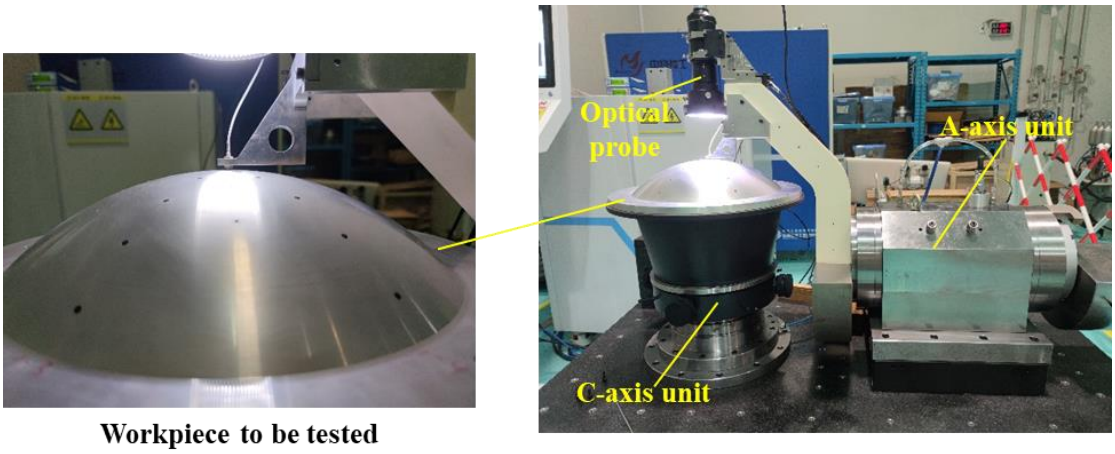

Figure 14. High-precision displacement sensors assisted in workpiece leveling and centering.

The specific operation steps shown in Figure 15 are as follows:

1. Set part parameters, including part name, part number, and part radius.
2. Use high-precision displacement sensors to measure the longitude contour, rotate the C-axis, and set the measurement range to 0~360°. After the measurement is completed, the collected contour lines will automatically be displayed in the longitude curve-drawing coordinate system. If the workpiece alignment is completed, the theoretical measurement result should be a straight line.
3. Use high-precision displacement sensors to measure the latitude contour, rotate the A-axis, and set the measurement range to −50~50°. After the measurement is completed, the collected contour lines will automatically be displayed in the latitude curve-drawing coordinate system. If the workpiece leveling is completed, the theoretical measurement result should be a straight line. Due to the possibility of passing through hole positions on the workpiece surface and introducing other errors during the measurement of longitude and latitude contours, the quality of the measured curves may deteriorate. Therefore, a curve fitting function is provided to obtain ideal contour lines.
4. Adjust the camera posture so that the center coordinates of the standard hole position of the workpiece coincide with the coordinate system "cross line" as much as possible.
5. After adjusting the pose of the workpiece and camera, click the "Set WCS" button to reset the workpiece coordinates of the current C-axis and A-axis to zero, and set them as the starting point for measurement, which is the measurement programming reference.

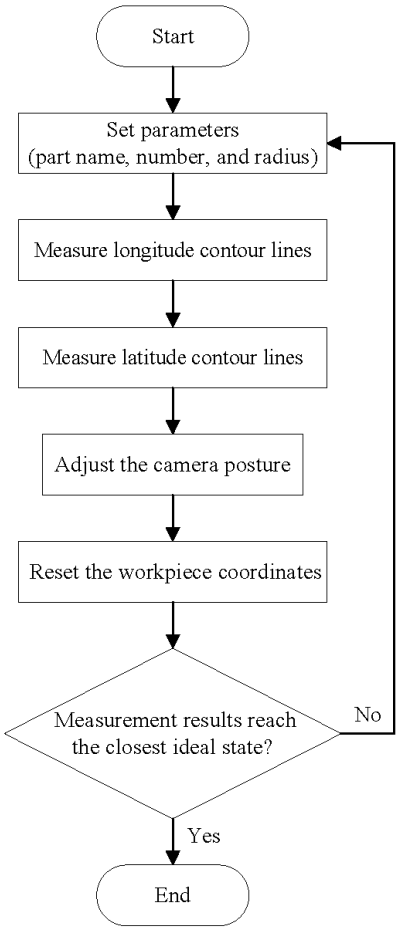

Figure 15. Flowchart of measurement operation.

In the actual measurement process, it is necessary to repeatedly adjust the pose of the workpiece and camera and repeat steps (1) to (4) until the measurement results reach the closest ideal state.

4.4. Measurement Result

Firstly, a three-coordinate machine to measure was used to contour the lines of different longitudes. The measurement errors of different latitudes (10°, 20°, 30°, and 40°) were calculated and used as agreed true values. The measurement results are shown in Table 4, and it can be seen that the maximum measurement error of the three-coordinate machine is 0.54′.

Table 4. Three-coordinate machine detection results (agreed true values).

Items Tested	Detection Results of the Three-Coordinate Machine (′)					
	Linear 1 (Longitude 0°)	**Linear 2 (Longitude 60°)**	**Linear 3 (Longitude 120°)**	**Linear 4 (Longitude 180°)**	**Linear 5 (Longitude 240°)**	**Linear 6 (Longitude 300°)**
Group 1: 6–10° ± 0.01° (latitude 10°)	0.12	0.06	0.06	0.12	0	0
Group 2: 6–10° ± 0.01° (latitude 20°)	−0.36	0.06	−0.06	−0.54	−0.18	−0.12
Group 3: 6–10° ± 0.01° (latitude 30°)	−0.3	0.12	0	−0.42	−0.06	0
Group 4: 6–10° ± 0.01° (latitude 40°)	−0.18	0.18	−0.06	−0.36	0.06	0

Then, the contour line error measurement was carried out by the proposed device. The five contour line measurement errors of different latitudes (10°, 20°, 30°, and 40°) are

shown in Figure 16, and the average values of the five measurement errors are recorded in Table 5.

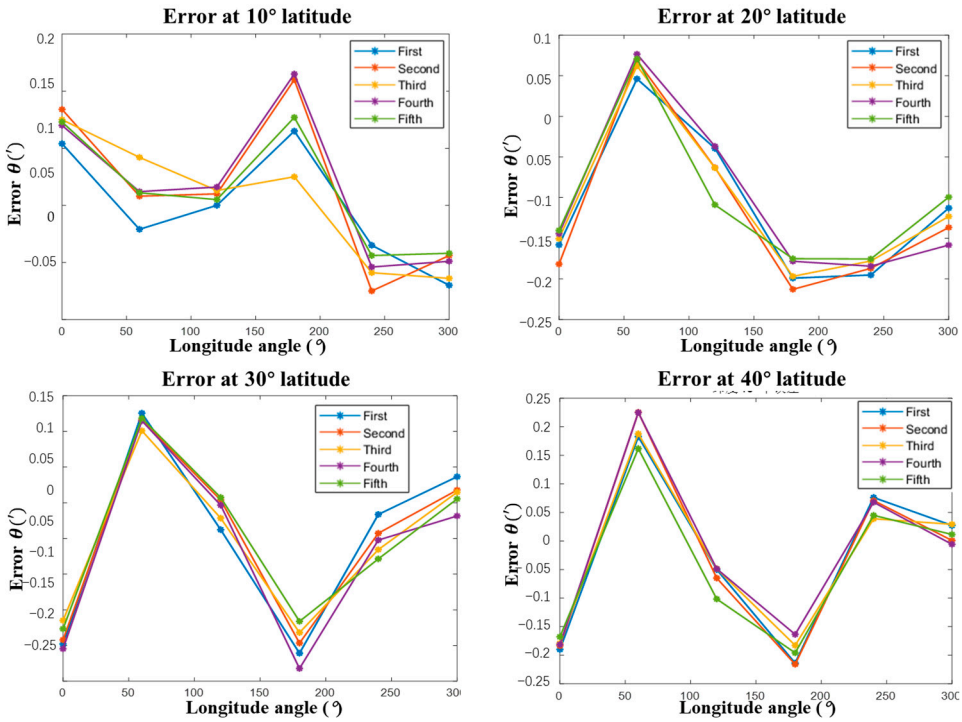

Figure 16. Five measurement results of the hole position error of different latitudes.

Table 5. Average of the five measurement results from the measuring machine (actual measured value).

Items Tested	Average of Five Angle Measurement Errors (′)					
	Linear 1 (Longitude 0°)	Linear 2 (Longitude 60°)	Linear 3 (Longitude 120°)	Linear 4 (Longitude 180°)	Linear 5 (Longitude 240°)	Linear 6 (Longitude 300°)
Group 1: 6–10° ± 0.01° (latitude 10°)	0.121	0.06	0.059	0.128	−0.003	−0.004
Group 2: 6–10° ± 0.01° (latitude 20°)	−0.155	0.065	−0.062	−0.192	−0.184	−0.126
Group 3: 6–10° ± 0.01° (latitude 30°)	−0.187	0.115	−0.01	−0.198	−0.051	0.011
Group 4: 6–10° ± 0.01° (latitude 40°)	−0.18	0.197	−0.063	−0.194	0.06	0.013

In order to evaluate the repeatability and stability of the five measurements, Class A uncertainty was calculated using Equation (32):

$$U_A = \sqrt{\frac{1}{N(N-1)}\sum_{i=1}^{N}(x_i - \overline{x})^2} \tag{32}$$

where U_A represents Class A uncertainty, N represents the number of measurement data points, x_i is the value of each data point, and $\overline{x}$ is the average value of this set of data. The uncertainty degree of the five contour measurement errors is shown in Table 6.

Table 6. Uncertainty degree of the five measurement results from the measuring machine.

Items Tested	Uncertainty of Five Angular Measurement Errors (″)					
	Linear 1 (Longitude 0°)	Linear 2 (Longitude 60°)	Linear 3 (Longitude 120°)	Linear 4 (Longitude 180°)	Linear 5 (Longitude 240°)	Linear 6 (Longitude 300°)
Group 1: 6–10° ± 0.01° (latitude 10°)	8.15	7.95	8.03	8.06	8.01	7.93
Group 2: 6–10° ± 0.01° (latitude 20°)	8.01	8.05	8.01	7.91	7.95	8.14
Group 3: 6–10° ± 0.01° (latitude 30°)	8.03	7.97	7.89	7.93	8.07	7.91
Group 4: 6–10° ± 0.01° (latitude 40°)	8.09	7.70	7.79	8.02	8.22	7.94

The measurement results indicate that the maximum error value of all hole system angles for a specific calibrated workpiece through a dedicated measuring device is 0.198′, and the maximum uncertainty value is 8.22″.

The measurement error of the device can be calculated by comparing its measurement results with those obtained from the coordinate measuring machine (CMM). In the measurement results shown in Table 7, it can be seen that the measurement accuracy of the dedicated measuring device for the angle of the spherical hole system is 0.348′, which meets the requirement that the spatial angle measurement error should not exceed 1′ during design.

Table 7. Comparison between the measurement results of this device and the results of the three-coordinate machine measurement.

Items Tested	Measured Value of This Device—Measured Value of Three Coordinates Machine (′)					
	Linear 1 (longitude 0°)	Linear 2 (longitude 60°)	Linear 3 (longitude 120°)	Linear 4 (longitude 180°)	Linear 5 (longitude 240°)	Linear 6 (longitude 300°)
Group 1: 6–10° ± 0.01° (latitude 10°)	0.001	0	−0.001	0.008	−0.003	−0.004
Group 2: 6–10° ± 0.01° (latitude 20°)	0.205	0.005	−0.002	0.348	−0.004	−0.006
Group 3: 6–10° ± 0.01° (latitude 30°)	0.113	−0.005	−0.01	0.222	0.009	0.011
Group 4: 6–10° ± 0.01° (latitude 40°)	0	0.017	−0.003	0.166	0	0.013

5. Conclusions

This study conducted a rapid and accurate measurement of spherical hole systems based on structural science and machine vision technologies. In addition, key technologies, such as measurement parameter definition, overall system design scheme, error modeling, and analysis, were introduced. A measurement system was built to conduct experimental verification research. The measurement results show that the maximum angle error of all hole systems for the specific calibrated workpiece through the dedicated measurement device is 0.198′, and the maximum uncertainty is 8.22″. The measurement error of this device can be obtained by subtracting the measurement results of the coordinate machine from the measurement results of this device. The measurement accuracy of the special measurement device for spherical hole angle is 0.348′, which meets the requirement of not exceeding 1′ for spatial angle measurement error during design. This research makes a meaningful contribution to the optical measurement of curved surface hole systems and advances the field of measurement science and technology.

Author Contributions: Conceptualization, P.W. and L.K.; methodology, P.W. and L.K.; software, P.W. and H.C.; validation, P.W.; formal analysis, P.W. and L.K.; investigation, P.W.; resources, P.W.; data curation, P.W.; writing—original draft preparation, P.W., L.K. and H.A.; writing—review and editing, H.A. and M.G.; visualization, H.A. and M.G.; supervision, L.K.; project administration, L.K.; funding acquisition, L.K. All authors have read and agreed to the published version of the manuscript.

Funding: This work was partially supported by the National Key Research and Development Program of China (No. 2022YFB3403404), the National Natural Science Foundation of China (Nos. 52322510 and 52075506), the Presidential Foundation of China Academy of Engineering Physics (YZJJZQ2022009), and the Natural Science Foundation of Sichuan of China (2023NSFSC1947).

Data Availability Statement: Data are contained within the article.

Conflicts of Interest: The authors declare no conflict of interest.

References

1. Tang, J.; Xu, X.; Zhou, G. A survey of measurement methods of the machine vision hole series coordinates on curved surface. *J. Mach.* **2006**, *11*, 3–5. (In Chinese)
2. Zhu, J.; Xu, X.; Wang, Y. Study on non-contacting measurement system for position of hole series by image processing. *J. Electr. Autom.* **2006**, *28*, 58–59. (In Chinese)
3. Huang, J.; Zhou, Z.; Deng, J.; Li J., G. High precision method to detect serial hole center coordinate based on circle fitting. *J. Tool Eng.* **2004**, *4*, 47–49. (In Chinese)
4. Huang, J.; Zhou, Z.; Yu, L. A precision measurement system based on linear array CCD used for hole series on curved surface. *J. Opto-Electron. Eng.* **2003**, *4*, 39–41. (In Chinese)
5. Yu, Z. Research on the Noncontact Measurement System of Spherical Circular Hole Series. Master's Thesis, Sichuan University, Chengdu, China, 18 April 2003.
6. Deng, J. The Measurement System of Spherical Circular Hole Series Basing on Machine Vision. Master's Thesis, Sichuan University, Chengdu, China, 20 April 2004.
7. Huang, J. Study on the Machine Vision Measure System for Position of Hole Series on Curved Surface. Ph.D. Thesis, Sichuan University, Chengdu, China, 8 April 2004.
8. Zhang, C.; Zhao, Z. Rapidly measuring system for ectopic holes based on laser displacement detection. *J. Mach. Build. Autom.* **2018**, *47*, 216–219. (In Chinese)
9. Xu, X. Study on the Fast and Precise Machine Vision System for the Hole-Positions on the Sphere Surface. Ph.D. Thesis, Sichuan University, Chengdu, China, 10 May 2006.
10. Sun, W.; Yi, J.; Ma, G. A vision-based method for dimensional in situ measurement of cooling holes in aero-engines during laser beam drilling process. *J. Int. J. Adv. Manuf. Technol.* **2022**, *119*, 3265–3277. [CrossRef]
11. Chen, X.; Longstaff, A.; Fletcher, S.; Myers, A. Analyzing and evaluating a dual-sensor autofocusing method for measuring the position of patterns of small holes on complex curved surfaces. *J. Sens. Actuators A-Phys.* **2014**, *210*, 86–94. [CrossRef]
12. Xu, S.; Huang, J.; Wang, D. Location measurement of holes on the spheroid part based on VC++ and Matlab. *J. Ordnance Ind. Autom.* **2005**, *2*, 31–32. (In Chinese)
13. Long, J. A device and Its Usage Method for Measuring the Accuracy of Centripetal Focusing Hole System. China Patent CN110006346A, 12 July 2019.
14. Chen, X.; Andrew, L.; Simon, F.; Myers, A. Deployment and evaluation of a dual-sensor autofocusing method for on-machine measurement of patterns of small holes on freeform surfaces. *J. Appl. Opt.* **2014**, *53*, 2246–2255. [CrossRef] [PubMed]
15. Li, M. The practice of the method used in measuring the location degree of the hole department by three coordinates. *J. Metrol. Meas. Tech.* **2008**, *35*, 27–28. (In Chinese)
16. Huang, F.; Yu, T.; Zhang, R. A new method for measuring the position error of hole system. *J. Agric. Mech. Res.* **2004**, *4*, 170–171. (In Chinese)
17. Huang, J.; Xu, B. A machine vision system for position measurement of small holes on the spherical surface. *J. Nanotechnol. Precis. Eng.* **2016**, *14*, 28–34.
18. Xie, S. Angle measurement of the large circular hole system. *J. Metrol. Meas. Tech.* **1996**, *2*, 5–7. (In Chinese)
19. Luo, T. The precision analysis of the measuring method for the holes centers distance in the workshop. *J. Mech. Res. Appl.* **2005**, *4*, 30–31. (In Chinese)
20. He, G.; Huang, X.; Guo, L.; Sang Y., C.; Huang, C. A Method for Detecting and Evaluating the Composite Positional Error of The Spherical Hole System. China Patent CN106568365A, 05 March 2019.
21. Wang, Y.; Ren, G.; Wu, B. Measuring the coaxiality of the hole system using a coordinate measuring machine. *J. Mod. Manuf. Technol. Equip.* **2000**, *1*, 39–40. (In Chinese)
22. Yu, H.; Zhao, Z.; Lu, Y. A Measurement System and Method for Coaxiality Error of a Reference-Free Hole System. China Patent CN104316001A, 28 January 2015.
23. Wu, E. Discussion on measuring tools of hole system in irregular-shaped parts. *J. Met. Work. Met. Cut.* **2008**, *17*, 49–51. (In Chinese)
24. Xu, K. The Key Technology Research of Multifunctional Probe about Big Distance of Porous Parts. Master's Thesis, Nanjing University of Aeronautics and Astronautics, Nanjing, China, March 2014.
25. Xu, B. Research on the Application of Surface Array CCD in Measuring the Coaxiality of the Hole System. Master's Thesis, Tianjin University, Tianjin, China, 1999.
26. Bieman, L. A novel method for spatial measurement of holes. *J. SPIE Opt. Illum. Image Sens. Mach. Vis.* **1987**, *728*, 116–122.

27. Gong, Y.; Seibel, E. Three-dimensional measurement of small inner surface profiles using feature-based 3-D panoramic registration. *J. Opt. Eng.* **2017**, *56*, 014108. [CrossRef]
28. Liu, Z. Research of Holes Position Measurement Method on a Curved Surface Based on Computer Vision. Master's Thesis, Huaqiao University, Quanzhou, China, 28 March 2014.
29. Gorpas, D.; Politopoulos, K.; Yova, D. A binocular machine vision system for three-dimensional surface measurement of small objects. *J. Comput. Med. Imaging Graph.* **2007**, *31*, 625–637. [CrossRef] [PubMed]
30. Malassiotis, S.; Strintzis, M. Stereo vision system for precision dimensional inspection of 3D holes. *J. Mach. Vis. Appl.* **2003**, *15*, 101–113. [CrossRef]
31. Zeng, Z.; Zhu, X.; Wang, J.; Li, X.; Lin, D. Effective area measurement of cartridges flash holes based on a machine vision system. *J. Mech. Sci. Technol. Aerosp. Eng.* **2016**, *35*, 40–43.
32. Gou, J.; Chen, X.; Ye, N.; Zhang L., Y. Development of on-machine vision inspection system for connection holes on aircraft parts. *J. Aeronaut. Manuf. Technol.* **2018**, *61*, 37–43. (In Chinese)
33. Fang, Z.; McGlure, V. Precision noncontact measurement of blind holes by machine vision technology. *J. SPIE Autom. Insp. Nov. Instrum.* **1997**, *3185*, 125–131.
34. Yang, W. The Application Research of Non-Contact Measurement for the Position of the Hole in a Spherical Surface and Digital Image Processing Technology. Master's Thesis, Sichuan University, Chengdu, China, 8 May 2004.
35. Kong, L. Development of Five-Axis Additive and Subtractive Hybrid Machining Center and Research on its Processing Technology. Master's Thesis, Xiamen University, Xiamen, China, June 2020.
36. Li, C.D. Research on the Identification Method of Geometric Error of Cradle Five-Axis NC Machine Tool. Master's Thesis, Harbin University of Science and Technology, Harbin, China, April 2020.
37. Yu, Z.Q. Research on Key Technologies of a Compound Measurement System Based on Multi-Sensor Information Fusion. Ph.D. Thesis, Tianjin University, Tianjin, China, December 2019.
38. Li, Z.T. Research on Online Inspection Technology of Robot Automatic Drilling Based on Vision. Master's Thesis, Harbin University of Science and Technology, Harbin, China, March 2021.